A Three-Dimensional Anelastic Model Based on the Vorticity Equation

JOON-HEE JUNG

Department of Atmospheric Science, Colorado State University, Fort Collins, Colorado

AKIO ARAKAWA

Department of Atmospheric and Oceanic Sciences, University of California, Los Angeles, Los Angeles, California

(Manuscript received 20 November 2006, in final form 10 April 2007)

ABSTRACT

A three-dimensional anelastic model has been developed using the vorticity equation, in which the pressure gradient force is eliminated. The prognostic variables of the model dynamics are the horizontal components of vorticity at all heights and the vertical component of vorticity and the horizontally uniform part of the horizontal velocity at a selected height. To implement the anelastic approximation, vertical velocity is diagnostically determined from the predicted horizontal components of vorticity by solving an elliptic equation. This procedure replaces solving the elliptic equation for pressure in anelastic models based on the momentum equation. Discretization of the advection terms uses an upstream-weighted partially third-order scheme. When time is continuous, the solution of this scheme is quadratically bounded. As an application of the model, interactions between convection and its environment with vertical shear are studied without and with model physics from the viewpoint of vorticity dynamics, that is, the deceleration/acceleration process of the basic flow in particular. The authors point out that the process is purely three-dimensional, especially when the convection is relatively localized, involving the twisting terms and the horizontal as well as vertical transports of vorticity. Finally, it is emphasized that parameterization of cumulus friction is a resolution-dependent problem of vorticity dynamics associated with cumulus convection.

1. Introduction

In the process of cloud modeling during the last decades, it was clearly realized that one- and two-dimensional cloud models are not capable of realistically simulating the complex behavior of convective systems. Since the 1970s, a number of three-dimensional cloud models have been developed to simulate the structure, intensity, and movement of convective clouds (Steiner 1973; Miller and Pearce 1974; Cotton and Tripoli 1978; Klemp and Wilhelmson 1978; Schlesinger 1978; Clark 1979; Takahashi 1981; Lipps and Hemler 1986; Redelsperger and Sommeria 1986; Tao and Soong 1986; Kogan 1991; Khairoutdinov and Randall 2003; and many others).

The three-dimensional cloud models developed so far can be classified into two families: one based on the anelastic system of equations and the other on the fully compressible system of equations. Whether they are anelastic or fully compressible, most of the three-dimensional cloud models formulate the dynamics of convection in the context of the momentum equation. In the anelastic models with the momentum equation, the pressure perturbation is calculated for a given motion field using a diagnostic elliptic equation. Complications involved in solving the elliptic equation can be eliminated in the fully compressible models. However, sound waves are retained in the system so that they must be appropriately handled computationally. A technique called "splitting," in which the sound wave modes are solved separately using a shorter time step than elsewhere in the model, is widely used in many compressible models (e.g., Klemp and Wilhelmson 1978).

The presence of vortical motions associated with convective clouds, however, leads us to examine the motions using the vorticity equation. The vorticity fields

Corresponding author address: Dr. Joon-Hee Jung, Department of Atmospheric Science, Colorado State University, Fort Collins, CO 80523-1371.
E-mail: jung@atmos.colostate.edu

DOI: 10.1175/2007MWR2095.1

associated with deep convective clouds have been *diagnostically* investigated by many authors (Schlesinger 1980; Cho and Clark 1981; Rotunno 1981; Tollerud and Esbensen 1983; Skamarock et al. 1994; Kirk 2003; Weisman and Rotunno 2004; and many others). Only a few nonhydrostatic three-dimensional models, on the other hand, use the vorticity equation as the prognostic equation (Thyer 1966; Sievers and Zdunkowski 1986; Saitoh et al. 1996; Thunis and Clappier 2000).

The reason that the three-dimensional vorticity equation has been seldom used in three-dimensional models is perhaps because its use requires a dynamics core that has a completely different logical structure from that of the conventional momentum equation models. For example, vorticity is by definition a nondivergent vector. How to maintain this constraint in a prognostic model is not obvious. Predicting the three components of vorticity everywhere is at least redundant or can even produce inconsistency. Also when we wish to use an anelastic approximation, a proper way to implement it in the vorticity equation framework needs to be found. In the momentum equation models, it is done through solving the elliptic equation for pressure. But, pressure is eliminated in vorticity equation models. Finally, since the horizontal components of the vorticity equation govern only the vertical shear of horizontal velocity, we need an algorithm to determine the vertically uniform part of the horizontal velocity.

One of the main purposes of this paper is to show how the vorticity equation can be used in the dynamics core of a three-dimensional model for nonhydrostatic nonacoustic motions. As an application of the model constructed using such a framework, the paper also presents a study of interactions between convection and its environment with vertical shear from the viewpoint of vorticity dynamics. Section 2 presents the description of the model emphasizing the logical structure of its dynamics core. Sections 3 and 4 discuss the results of idealized experiments without physics and those of the ensemble cloud simulation with full physics. Finally, the summary and conclusions are presented in section 5.

2. Model description

a. The dynamical framework

An anelastic system of the continuity and momentum equations is given in Lipps and Hemler (1982). With the Cartesian coordinates, these equations may be written as

$$\frac{\partial}{\partial x}(\rho_0 u) + \frac{\partial}{\partial y}(\rho_0 v) + \frac{\partial}{\partial z}(\rho_0 w) = 0, \tag{1}$$

$$\frac{du}{dt} - fv = -\frac{\partial}{\partial x}(c_p\theta_{v0}\pi') - \frac{\partial}{\partial x}(\overline{u''u''}) - \frac{\partial}{\partial y}(\overline{u''v''}) - \frac{1}{\rho_0}\frac{\partial}{\partial z}(\rho_0\overline{u''w''}), \tag{2}$$

$$\frac{dv}{dt} + fv = -\frac{\partial}{\partial y}(c_p\theta_{v0}\pi') - \frac{\partial}{\partial x}(\overline{u''v''}) - \frac{\partial}{\partial y}(\overline{v''v''}) - \frac{1}{\rho_0}\frac{\partial}{\partial z}(\rho_0\overline{v''w''}), \quad \text{and} \tag{3}$$

$$\frac{dw}{dt} = -\frac{\partial}{\partial z}(c_p\theta_{v0}\pi') + g\left(\frac{\theta'}{\theta_0} + 0.61q_v - q_c - q_i - q_r - q_s - q_{\rm gr}\right) - \frac{\partial}{\partial x}(\overline{u''w''}) - \frac{\partial}{\partial y}(\overline{v''w''}) - \frac{1}{\rho_0}\frac{\partial}{\partial z}(\rho_0\overline{w''w''}). \tag{4}$$

Here u, v, and w are the x, y, and z components of velocity, respectively; ρ is the density; f is the Coriolis parameter; g is the gravitational acceleration; θ is the potential temperature; θ_v is the virtual potential temperature defined by $\theta_v \equiv \theta(1 + 0.61q_v)$; and q is the mixing ratio of water vapor (v), cloud water (c), cloud ice (i), rainwater (r), snow (s), or graupel (gr). In these equations, variables with a subscript 0 refer to a hydrostatic reference state, which varies in z only. The Coriolis force is simplified by omitting its component that depends on the cosine of latitude. A single prime indicates the departure from the reference state and double primes indicate turbulence-scale velocity components. The nondimensional pressure π is given by $\pi = (p/p_{00})^{R/c_p}$, where p is the pressure, p_{00} is a constant reference pressure, R is the gas constant for dry air, and c_p is the specific heat of dry air. The operator d/dt denotes the material time derivative, which can be expressed for a variable A as

$$\frac{dA}{dt} = \frac{\partial A}{\partial t} + u\frac{\partial A}{\partial x} + v\frac{\partial A}{\partial y} + w\frac{\partial A}{\partial z}. \tag{5}$$

The logical structure of the model dynamics is quite different from most of the existing three-dimensional models because the vorticity equation is used as the prognostic equation instead of the momentum equation. We first define the x, y, and z components of vorticity by

$$\xi \equiv \frac{\partial w}{\partial y} - \frac{\partial v}{\partial z}, \quad \eta \equiv \frac{\partial u}{\partial z} - \frac{\partial w}{\partial x}, \quad \text{and} \quad \zeta \equiv \frac{\partial v}{\partial x} - \frac{\partial u}{\partial y}, \tag{6}$$

respectively. The vorticity components defined by (6) identically satisfy the nondivergence of the three-dimensional vorticity given by

$$\frac{\partial \xi}{\partial x} + \frac{\partial \eta}{\partial y} + \frac{\partial \zeta}{\partial z} = 0. \tag{7}$$

From (2), (3), and (4), the x, y, and z components of the vorticity equation can be derived as

$$\frac{\partial \xi}{\partial t} = -\left[\frac{\partial}{\partial x}(u\xi) + \frac{\partial}{\partial y}(v\xi) + \frac{\partial}{\partial z}(w\xi)\right] + \xi\frac{\partial u}{\partial x} + \eta\frac{\partial u}{\partial y} + \zeta\frac{\partial u}{\partial z} + f\frac{\partial u}{\partial z} + \frac{\partial B}{\partial y} + \frac{\partial F_w}{\partial y} - \frac{\partial F_v}{\partial z}, \tag{8}$$

$$\frac{\partial \eta}{\partial t} = -\left[\frac{\partial}{\partial x}(u\eta) + \frac{\partial}{\partial y}(v\eta) + \frac{\partial}{\partial z}(w\eta)\right] + \eta\frac{\partial v}{\partial y} + \xi\frac{\partial v}{\partial x} + \zeta\frac{\partial v}{\partial z} + f\frac{\partial v}{\partial z} - \frac{\partial B}{\partial x} - \frac{\partial F_w}{\partial x} + \frac{\partial F_u}{\partial z}, \quad \text{and} \tag{9}$$

$$\frac{\partial \zeta}{\partial t} = -\left[\frac{\partial}{\partial x}(u\zeta) + \frac{\partial}{\partial y}(v\zeta) + \frac{\partial}{\partial z}(w\zeta)\right] + \zeta\frac{\partial w}{\partial z} + \xi\frac{\partial w}{\partial x} + \eta\frac{\partial w}{\partial y} - f\left(\frac{\partial u}{\partial x} + \frac{\partial v}{\partial y}\right) + \frac{\partial F_v}{\partial x} - \frac{\partial F_u}{\partial y}, \tag{10}$$

where B is the buoyancy given by $g(\theta'/\theta_0 + 0.61q_v - q_c - q_i - q_r - q_s - q_{gr})$; and F_u, F_v, and F_w are the turbulent flux convergence terms in the right-hand sides of (2), (3), and (4), respectively. In (8), (9), and (10), the first term after the brackets represents the stretching effect and the two subsequent terms represent the twisting effect.

Because the vertical derivative of ζ is diagnostically related to the ξ and η fields through (7), it is not necessary to predict the ζ field using (10) except at an arbitrarily selected height, z_T. The ζ field at an arbitrary height z can then be obtained through

$$\zeta_z = -\int_{z_T}^{z}\left(\frac{\partial \xi}{\partial x} + \frac{\partial \eta}{\partial y}\right)dz + \zeta_{z_T}. \tag{11}$$

Thus, while (8) and (9) are applied everywhere, we apply (10) only at the selected height. In the model, the upper boundary is chosen as the height z_T. It can be shown that the three-dimensional vorticity field predicted by (8), (9), and (11) is consistent with the prediction using (10).

After predicting the horizontal components of the vorticity using (8) and (9), we update the vertical velocity. Operating $\partial/\partial x$ on η and $\partial/\partial y$ on ξ in (6), we obtain

$$\frac{\partial^2 w}{\partial x^2} - \frac{\partial^2 u}{\partial x \partial z} = -\frac{\partial \eta}{\partial x} \quad \text{and} \quad \frac{\partial^2 w}{\partial y^2} - \frac{\partial^2 v}{\partial y \partial z} = \frac{\partial \xi}{\partial y}. \tag{12}$$

With the anelastic continuity Eq. (1), the sum of two equations in (12) becomes

$$\left(\frac{\partial^2}{\partial x^2} + \frac{\partial^2}{\partial y^2}\right)w + \frac{\partial}{\partial z}\left[\frac{1}{\rho_0}\frac{\partial}{\partial z}(\rho_0 w)\right] = -\frac{\partial \eta}{\partial x} + \frac{\partial \xi}{\partial y}. \tag{13}$$

For a given vorticity field, we can determine w by solving the three-dimensional elliptic equation in (13) with the upper and lower boundary conditions for w.

To update the horizontal velocity at a selected height $z = z_T$, which is chosen to be the upper boundary in the model, we divide the velocity into the rotational and divergent parts through

$$u = u_\psi + u_\chi \quad \text{and} \quad v = v_\psi + v_\chi, \tag{14}$$

where

$$u_\psi = -\frac{\partial \psi}{\partial y}, \quad u_\chi = \frac{\partial \chi}{\partial x}, \quad v_\psi = \frac{\partial \psi}{\partial x}, \quad \text{and} \quad v_\chi = \frac{\partial \chi}{\partial y}. \tag{15}$$

The streamfunction Ψ is updated solving the two-dimensional elliptic equation

$$\frac{\partial^2 \psi}{\partial x^2} + \frac{\partial^2 \psi}{\partial y^2} = \zeta. \tag{16}$$

The velocity potential χ, on the other hand, is obtained from the solution of

$$\left(\frac{\partial^2}{\partial x^2} + \frac{\partial^2}{\partial y^2}\right)\chi = -\frac{1}{\rho_0}\frac{\partial}{\partial z}(\rho_0 w) \tag{17}$$

using the vertical velocity w updated by (13). We may predict the horizontally uniform part of the horizontal velocity by

$$\frac{\partial \overline{u}^{xy}}{\partial t} = -\frac{1}{\rho_0}\frac{\partial}{\partial z}(\rho_0 \overline{uw}^{xy}) + \overline{fv}^{xy} - \overline{\frac{\partial}{\partial x}(c_p \theta_{v0} \pi')}^{xy} + \overline{F}_u^{xy} \quad \text{and} \tag{18}$$

$$\frac{\partial \overline{v}^{xy}}{\partial t} = -\frac{1}{\rho_0}\frac{\partial}{\partial z}(\rho_0 \overline{vw}^{xy}) - \overline{fu}^{xy} - \overline{\frac{\partial}{\partial y}(c_p \theta_{v0} \pi')}^{xy} + \overline{F}_v^{xy}, \tag{19}$$

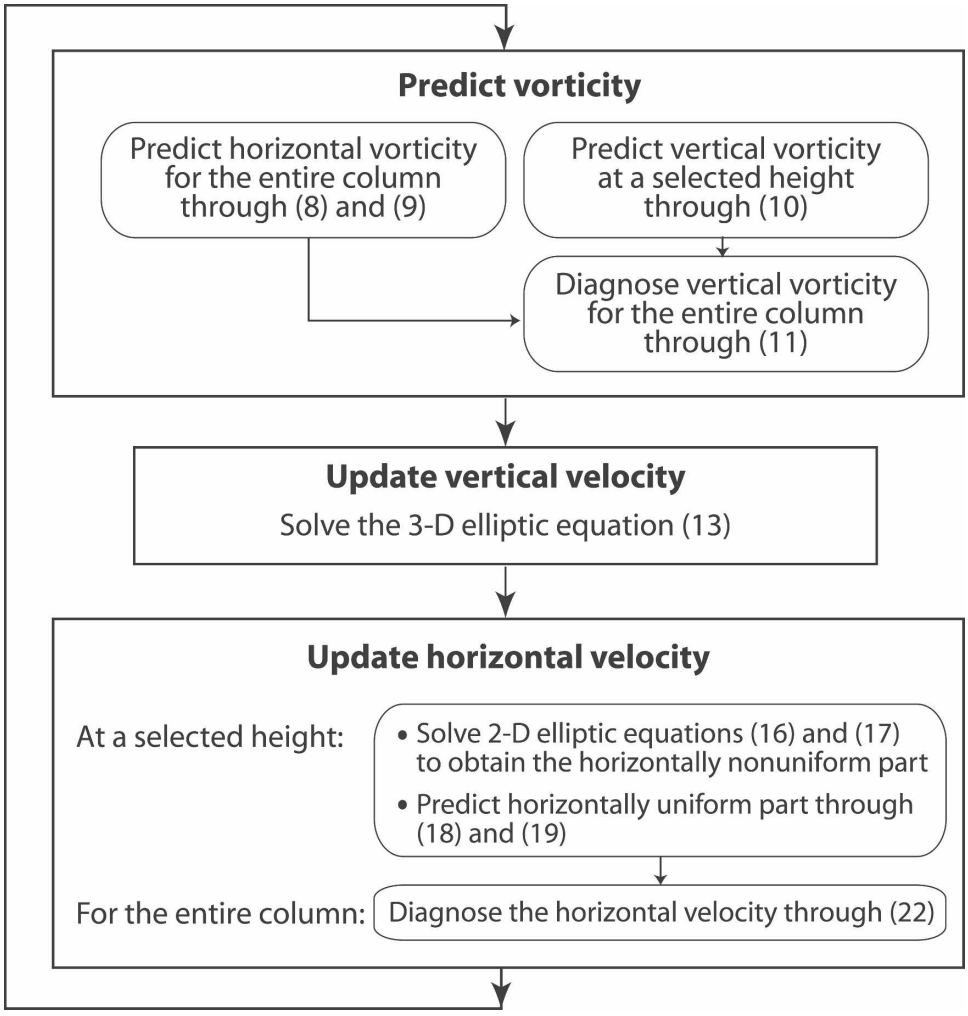

FIG. 1. Flowchart of the model structure for predicting dynamical variables.

where $\overline{()}^{xy}$ represents the horizontal average. Using these horizontally uniform and nonuniform parts, the horizontal velocities at $z = z_T$ are given as

$$u_T = \overline{u}^{xy} + u_\psi + u_\chi, \quad v_T = \overline{v}^{xy} + v_\psi + v_\chi. \tag{20}$$

To update the horizontal velocity components at an arbitrary height z, we use (6) rewritten as

$$\frac{\partial u}{\partial z} = \frac{\partial w}{\partial x} + \eta \quad \text{and} \quad \frac{\partial v}{\partial z} = \frac{\partial w}{\partial y} - \xi. \tag{21}$$

Integrating (21) with respect to z downward, we obtain

$$u = \int_{z_T}^{z} \left(\frac{\partial w}{\partial x} + \eta \right) dz + u_T(x, y, t) \quad \text{and}$$

$$v = \int_{z_T}^{z} \left(\frac{\partial w}{\partial y} - \xi \right) dz + v_T(x, y, t). \tag{22}$$

The model described above is quite different from that used in Thunis and Clappier (2000). In their model, a pair of two-dimensional elliptic equations for the streamfunction are iteratively solved. In our model, a single three-dimensional elliptic equation for the vertical velocity is solved instead. The use of this equation is one of the unique aspects of the model described in this paper. Figure 1 presents a flowchart of the logical structure of the model dynamics. The major points here are satisfying the nondivergence of the three-dimensional vorticity given by (7) and the way in which the velocity field is updated from the predicted vorticity field.

The thermodynamic equation in the model is given by

$$\frac{d\theta}{dt} = \left(\frac{\partial \theta}{\partial t} \right)_{\text{MP}} + \left(\frac{\partial \theta}{\partial t} \right)_{\text{RAD}} + \left(\frac{\partial \theta}{\partial t} \right)_{\text{TUR}} + \left(\frac{\partial \theta}{\partial t} \right)_{\text{LS}}, \tag{23}$$

where the tendency terms with the subscripts MP, RAD, and TUR represent the sources due to microphysics, radiation, and turbulent flux convergence, respectively. The tendency term with subscript LS represents a forcing due to prescribed large-scale advection. The budget equations for water vapor and nonprecipitating water species (cloud water and cloud ice), and for precipitating water species (rain, snow and graupel) can be, respectively, written by

$$\frac{dq_{\rm np}}{dt} = \left(\frac{\partial q_{\rm np}}{\partial t}\right)_{\rm MP} + \left(\frac{\partial q_{\rm np}}{\partial t}\right)_{\rm TUR} + \left(\frac{\partial q_{\rm np}}{\partial t}\right)_{\rm LS} \tag{24}$$

and

$$\frac{dq_p}{dt} = \frac{1}{\rho_0}\frac{\partial}{\partial z}(\rm PF) + \left(\frac{\partial q_p}{\partial t}\right)_{\rm MP} + \left(\frac{\partial q_p}{\partial t}\right)_{\rm TUR}. \tag{25}$$

In these equations, the tendency term with the subscript MP represents conversions between species due to microphysics. In (25), PF represents precipitation fluxes. In the current model, we ignore the turbulent fluxes of precipitating water.

b. Discretization

The main variables and their locations in the vertical and horizontal grids are shown in Fig. 2. All thermodynamic variables are located at the θ point. This vertical grid structure, which is similar to the Lorenz grid in quasistatic models, is not the best vertical grid in simulating hydrostatic adjustment in nonhydrostatic models with an Eulerian vertical grid. But it has been chosen in this model to maintain the continuity from its two-dimensional predecessor. In the vertical, we usually use a stretched vertical grid described by Krueger (1988) to increase the vertical resolution near the surface.

The space-difference scheme for advecting scalar variables and vorticity components is an Eulerian scheme, which has the third-order accuracy when the flow is uniform. When time is continuous, solutions of this scheme are quadratically bounded. In discretizing the flux convergence terms in (8) and (9), which are applied to the entire column, and in (10), which is applied to a selected height, we take the advantage of using the vorticity equation by directly implementing computational constraints on the enstrophy change under advection processes. For more details on the discretization, see Jung and Arakawa (2005). The three-dimensional elliptic equation in (13) is solved with the condition $w = 0$ at the lower and upper boundaries using centered finite differences with the stretched vertical coordinate. The resulting tridiagonal linear system

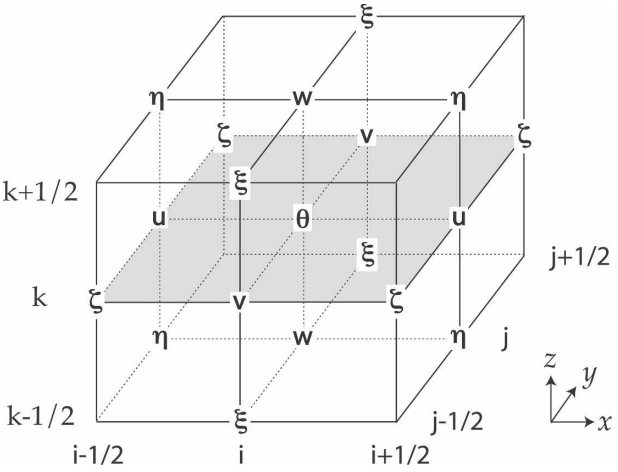

FIG. 2. A three-dimensional view of the model grids.

is then solved using the FISHPAK (a package of FORTRAN subprograms for the solution of separable elliptic partial differential equations) of the University Corporation for Atmospheric Research (UCAR) for solving separable elliptic partial differential equations by the direct, Fourier series method. The second-order Adams–Bashforth scheme is used for time differencing except that the first-order backward scheme is used for the buoyancy and turbulence terms and the first-order forward scheme is used for the physics terms. The second-order Adams–Bashforth scheme is unstable, but its growth rate depends on the time step used. Since sufficiently short time steps are used in the experiments described in sections 3 and 4, the actual growth is negligible with the amount of dissipation included in the model. The properties of the underlying surface required by the model are temperature, wetness, and roughness length. Currently, all three are prescribed. In the experiments reported in this paper, the upper and lower boundaries are rigid horizontal planes and the horizontal domain is cyclic.

c. Physical parameterizations

The physical parameterizations in the model include a three-phase microphysical parameterization (Krueger et al. 1995; Lin et al. 1983; Lord et al. 1984), a radiative transfer parameterization (Fu et al. 1995), a surface flux parameterization (Deardorff 1972), and a first-order turbulence closure that uses eddy viscosity and diffusivity coefficients depending on deformation and stability (Shutts and Gray 1994). Except for the turbulence parameterization, these physical parameterizations are essentially the same as those in the two-dimensional cloud model originally developed by Krueger (1988), which has been applied to a variety of cloud regimes including stratocumulus, altocumulus, cumulonimbus,

and cirrus clouds (see, e.g., Krueger 2000). Additionally, the model has a Newtonian-type cooling above the 10-km height and a Rayleigh-type friction in the top five layers.

3. Idealized experiments without physics

All experiments described in this section are performed without physics and Coriolis force. Instead of the stretched vertical grid described in section 2, a uniform vertical grid is used in these experiments.

a. Cold bubble experiment

The design of the cold bubble experiment follows the setup of Straka et al. (1993), which was originally used as a benchmark problem for two-dimensional nonhydrostatic models. The same experimental setup is adopted for the sake of comparison, but the simulation is carried out using the three-dimensional model we developed with no variation in the y direction.

In this setup, an initial cold disturbance is introduced to a neutrally stratified resting atmosphere as

$$\Delta T = \begin{cases} 0 & \text{if} \quad L > 1, \\ -15[\cos(\pi L) + 1]/2 & \text{if} \quad L \le 1, \end{cases} \tag{26}$$

where $L \equiv \{[(x - x_c)/x_r]^2 + [(z - z_c)/z_r]^2\}^{1/2}$, $x_c = 0$ km, $x_r = 4$ km, $z_c = 3$ km, and $z_r = 2$ km. The horizontal domain extends from -19 to 19 km and its height is 6.4 km. The grid size is 25, 50, 100, 200, or 400 m. The integration time step is 1 s with the grid size greater than 50 m and smaller otherwise. As in Straka et al. (1993), a constant diffusion coefficient, 75 $m^2\ s^{-1}$, is used for both vorticity and scalar prognostic equations.

The model is integrated over a 900-s period. The θ' field from the simulation at $t = 900$ s is shown in Fig. 3 for different grid sizes. From the results with high resolution, it is seen that three Kelvin–Helmholtz shear instability rotors develop along the top boundary of the simulated cold air outflow. These results show a good agreement with the reference solution in Straka et al. (1993).

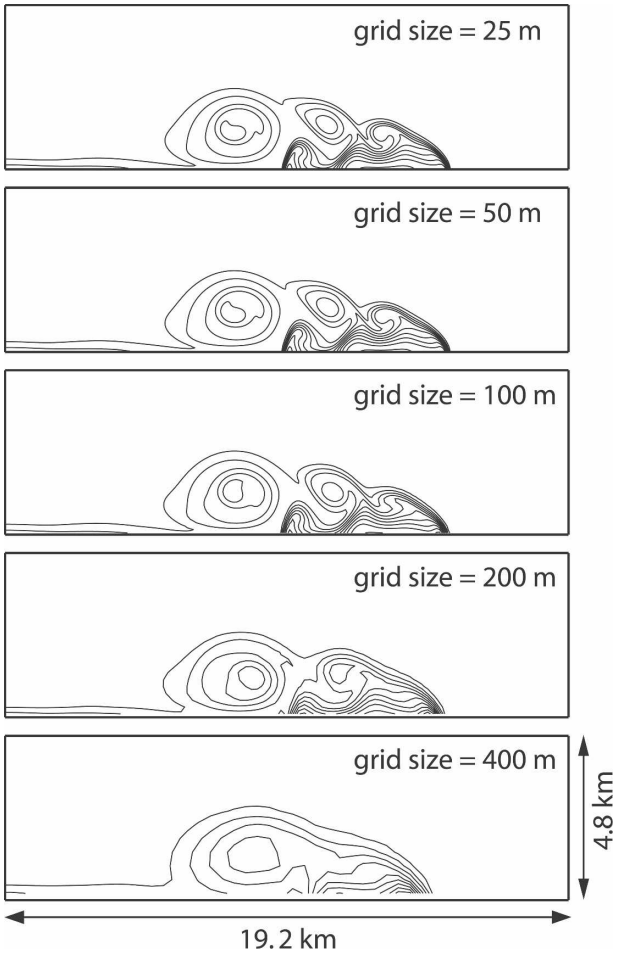

FIG. 3. The x–z cross sections of θ' at $t = 900$ s obtained from the simulations "using the setup of Straka et al. (1993)" with grid sizes of 25, 50, 100, 200, and 400 m. The contour interval is 1°C. All contours are centered around the zero contours. (Note that only a portion of the domain is shown.)

b. Warm bubble experiments

To demonstrate the performance of the model as well as to gain better understanding of the three-dimensional interactions of convection with the basic flow from the viewpoint of vorticity dynamics, we have performed a series of idealized experiments simulating the time evolution of thermals in various environmental conditions. In these experiments, a 250-m grid size is used in every direction. The horizontal domain is 32 km × 32 km and the vertical domain is 15 km deep. To obtain the initial motion fields that satisfy the discrete anelastic continuity equation of the model, we perform a short-term (3 min) presimulation. In this simulation, an ellipsoidal form of potential temperature perturbation was prescribed as

$$\Delta\theta = \begin{cases} 0 & \text{if} \quad L > 1, \\ \Delta\theta_{\max}(1 - L)/\rho_o(z) & \text{if} \quad L \le 1, \end{cases} \tag{27}$$

where $\Delta\theta_{\max} = 4$ K, $L \equiv \{[(x - x_c)/x_r]^2 + [(y - y_c)/y_r]^2 + [(z - z_c)/z_r]^2\}$, $x_c = 15.875$ km, $x_r = 4$ km, $y_c = 15.875$ km, $y_r = 4$ km, $z_c = 2.5$ km, and $z_r = 2$ km. We then ran the model from the resting state while fixing the location and buoyancy of the thermal. The prescribed thermal and motion fields developed at $t = 3$ min are used for the initial condition for the following experiments.

1) EXP1

This experiment is designed to further examine the performance of the advection scheme. Neither buoyancy nor diffusion is included in this experiment. In this experiment, the initial vorticity field is simply advected with possible stretching/shrinking effects in the azimuthal direction. Since there is no background shear, the solution should remain approximately axisymmetric in time. (Because of the use of a square grid with cyclic boundary conditions, the axisymmetry is not exactly maintained.)

Figure 4 shows the simulated potential vorticity fields. Here "potential vorticity" is defined as the azimuthal component of vorticity divided by density and the distance from the axis of axisymmetry representing the azimuthal stretching effect on vorticity. Since neither buoyancy nor diffusion is included, this quantity is supposed to be conserved with respect to a material element for an axisymmetric flow when time is continuous. It is seen in Fig. 4 that the potential vorticity of the thermal seems to be well conserved as it rises. In Fig. 5, we show the mass-weighted three-dimensional domain-averaged kinetic energy, enstrophy, and potential enstrophy as functions of time. We see that the kinetic energy is practically conserved throughout the experiment while the potential enstrophy slowly decreases in time. The relatively rapid decreases near the beginning and end of the experiments are due to the existence of small-scale components in the initial condition and the generation of those components by the complex interference between the approximately axisymmetric flow and the square geometry of the domain, respectively. In contrast to the potential enstrophy, the enstrophy increases with time. Figure 5b shows that this increase is almost entirely due to the physical effects of stretching and twisting.

2) EXP2 AND EXP2S

To test the performance of the model for purely three-dimensional situations and to understand some of the basic interactions between a thermal and basic flow, two experiments are performed: EXP2 initially with no basic flow and EXP2S initially with a horizontally uniform basic flow with vertical shear. Unlike EXP1, the buoyancy and the diffusion with a constant coefficient 100 $m^2\ s^{-1}$ are included in these experiments. The initial conditions consist of a neutral environment and a disturbance prepared in the same way as in EXP1, but using a rather weak initial potential temperature perturbation with $\Delta\theta_{max} = 1$ K. For EXP2S, a horizontally uniform westerly wind (u_0) that linearly increases from

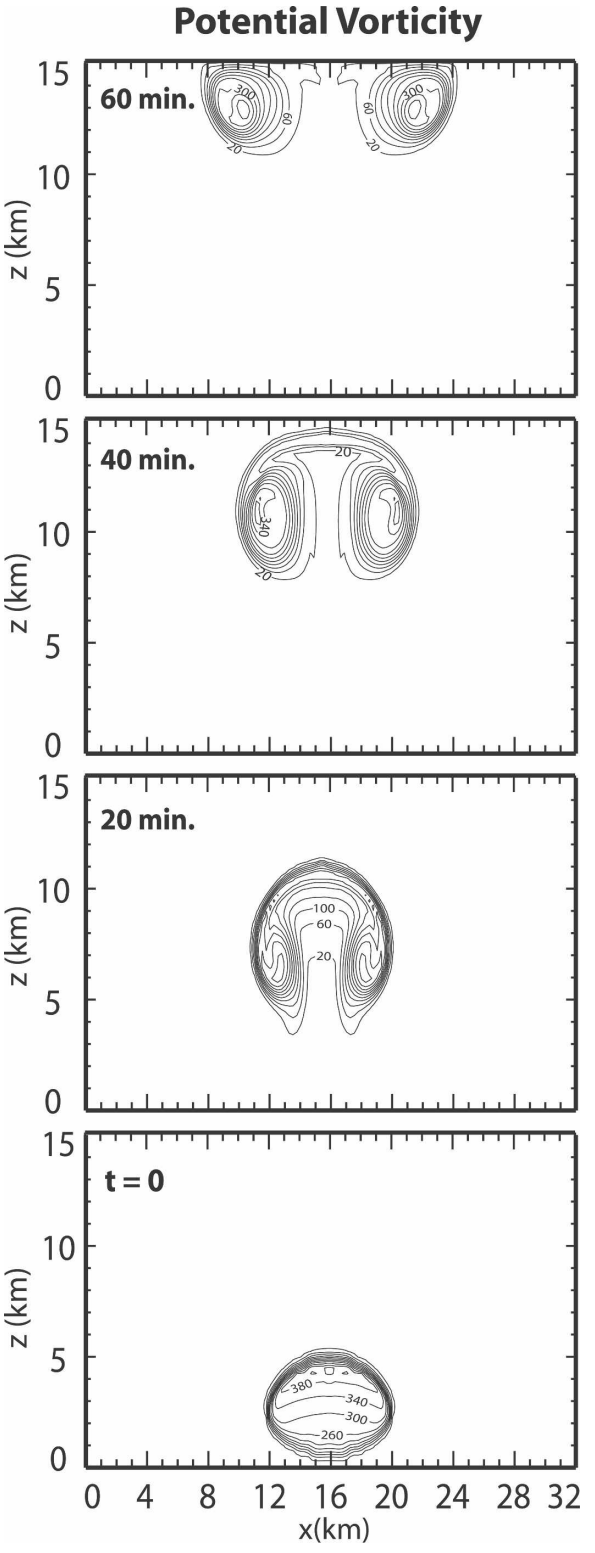

FIG. 4. Time evolution of the simulated potential vorticity fields on the x–z cross section at the center of the y domain obtained from EXP1. The contour interval is $40 \times 10^{-4}\ s^{-1}$.

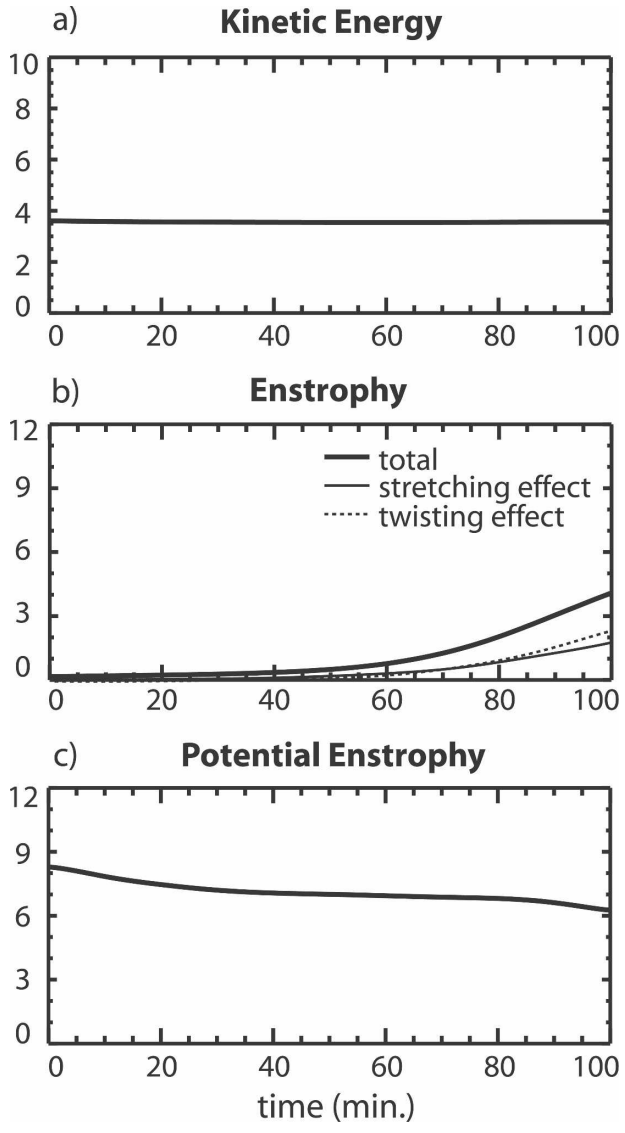

FIG. 5. The mass-weighted three-dimensional domain-averaged (a) kinetic energy, (b) enstrophy, and (c) potential enstrophy obtained from EXP1. In (b), the stretching and twisting effects are individually shown as well as the total effects.

0 at the surface to 10 m s^{-1} at 15-km height is added to the initial wind field.

In these simulations, the initial thermal rises due to the buoyancy in the neutral atmosphere until it reaches the upper boundary. With the shear in the basic flow, the thermal is slanted with height and thus its axisymmetry is not maintained even approximately. To further examine the motion field associated with the thermal, Fig. 6 shows η^* ($\equiv\eta/\rho_o$) on the x–z cross section at the center of the y domain obtained from EXP2 (left) and EXP2S (right). Dashed lines represent negative values. The updraft and downdraft are shaded with light gray and dark gray, respectively. In the right panels (EXP2S), the value of η_0^* ($\equiv\rho_0^{-1}\partial u_0/\partial z$) due to the shear of the initial basic flow is subtracted. In the figure, it can be seen that without shear, positive (clockwise) and negative (counterclockwise) vortices symmetrically develop around the updraft. With shear, on the contrary, asymmetry appears between the positive and negative vortices due to the downward stretching of the negative vortex at the upwind side and the upward shrinking of the positive vortex at the downwind side. Thus, it is clear that the net vertical transport of η^* is zero in EXP2 and dominantly positive (upward) in EXP2S at this y. As we show quantitatively later in (28), the upward transport of η^* means a tendency toward deceleration of the westerly flow. The corresponding zonal wind field obtained from EXP2S is shown in Fig. 7. Here, the initial basic flow (u_0) is subtracted. It can be clearly seen that the zonal wind is decelerated at this y representing the active updraft/downdraft region.

Figure 8 shows horizontal cross sections of ζ^* ($\equiv\zeta/\rho_o$; left) and the zonal wind (right) at 5-, 8-, and 13-km heights from EXP2S. In the figure, we see that positive vorticity (counterclockwise in the figure) develops on the right side of the updraft relative to the shear vector. On the left side of the updraft, on the other hand, negative vorticity (clockwise) develops. Similar vorticity couplets associated with cloud clusters in shear flow have been observed by many authors (e.g., Schlesinger 1980; Cho and Clark 1981; Rotunno 1981; Tollerud and Esbensen 1983). The zonal wind field shows corresponding local deceleration in the active updraft/downdraft regions and compensating local acceleration in convectively inactive regions. At least at the middle levels (z = 5 and 8 km), these local deceleration and acceleration tend to compensate when the horizontal average is taken over the entire model domain.

The deceleration/acceleration patterns shown in the right panels of Fig. 8 have pronounced structures in y. To further investigate such y dependencies in a concise way, we show the zonal averages of the three components of wind (left) and vorticity divided by density (right) for t = 26 min on a y–z plane in Fig. 9. In the figure, dashed lines represent negative values. The ξ^* ($\equiv\xi/\rho_o$) field in Fig. 9d shows a direct circulation generated by the buoyancy associated with the thermal. It is consistent with the lower-level convergence and upper-level divergence in the y component of wind (Fig. 9b) and the updraft at the center of the y domain (Fig. 9c). Unlike the ξ^* field, the ($\eta^* - \eta_o^*$) field in Fig. 9e shows a vertical arrangement of positive and negative values. This is consistent with the asymmetry of the positive and negative vortices shown in the lower-right panel in Fig. 6. Along with the couplet of ζ^* shown in

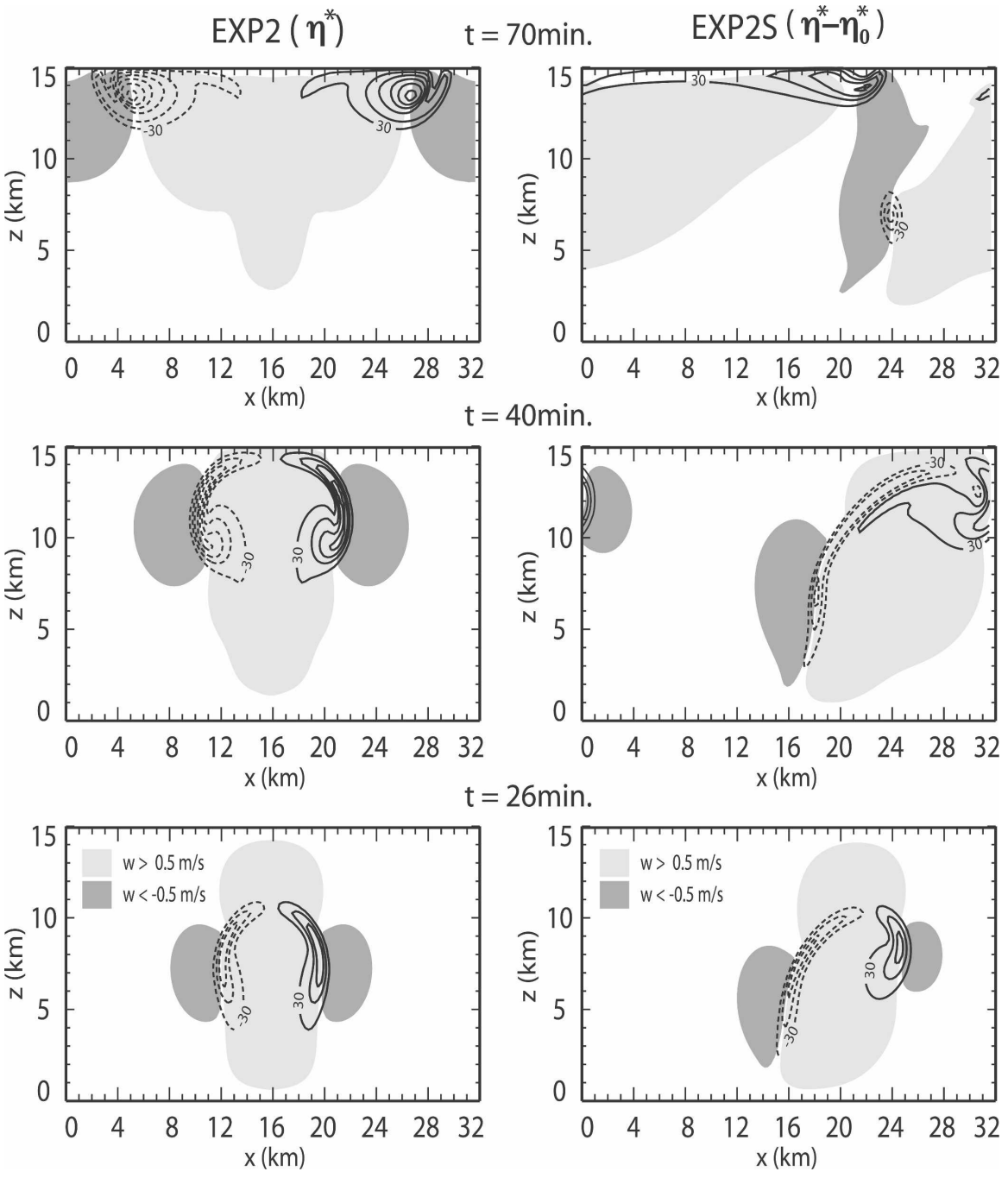

FIG. 6. The η^* ($\equiv \eta/\rho_o$) fields on the x–z cross section at the center of the y domain obtained from (left) EXP2 and (right) EXP2S. Here $\eta_0^* \equiv \rho_0^{-1}\partial u_0/\partial z$ and u_0 represent the initial basic flow. Solid and dashed lines represent positive and negative values, respectively. The contour interval is 60×10^{-4} m^3 kg^{-1} s^{-1}. The updraft and downdraft are shaded light gray and dark gray, respectively.

Fig. 9f, the vertical arrangement of η^* is also consistent with the local deceleration of zonal wind that has a maximum around the 5-km height.

As shown in Fig. 9, the motion field associated with the thermal is fully three-dimensional and all of the three components of vorticity are involved when there is a shear in the basic flow. The time change of vorticity depends on the flux convergence (divergence), stretching and twisting, diffusion, and buoyancy effects. Among these, dominant individual effects for the generation of the ξ^*, $(\eta^* - \eta_o^*)$, and ζ^* fields shown in Fig. 9 are plotted in Fig. 10. These are accumulated effects

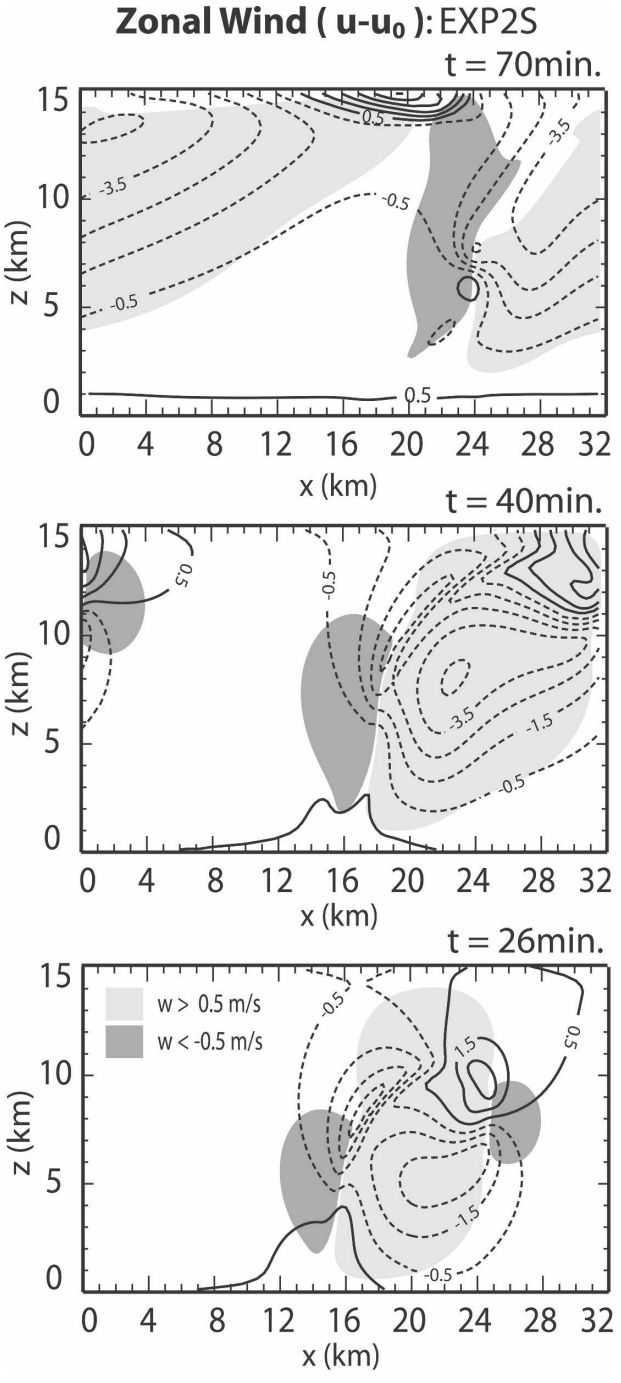

FIG. 7. The zonal wind on the x–z cross section at the center of the y domain obtained from EXP2S. The initial basic flow (u_0) is subtracted from the field. Solid and dashed lines represent positive and negative values, respectively. The contour interval is 1 m s^{-1}. The updraft and downdraft are shaded light gray and dark gray, respectively.

from $t = 0$ to $t = 26$ min. The figure shows that the main source term for the generation of the ξ^*field (top panels) is the buoyancy. For the η^* field (middle panels) and ζ^* field (bottom panels), the twisting term is the main source. Circulation carries the generated ξ^* and ζ^* from the lower levels to the upper levels and η^* inward and upward through the flux convergence and divergence, respectively.

So far, the simulated results from EXP2S are interpreted in view of the three-dimensional vorticity dynamics, which governs the redistribution and reorientation of the three-dimensional vorticity and the associated change of the velocity fields. Figure 11, on the other hand, shows a diagnosis of the results based on the more standard viewpoint of the momentum dynamics. In this figure, the zonal averages of the vertical and zonal winds (top panels) and the vertical eddy momentum flux (bottom panel) from EXP2S are presented on the z–t cross sections at the center of the y domain. With time, the thermal rises and strong updraft appears at the upper levels (Fig. 11a). As the updraft develops, the momentum is transported downward by the thermal (Fig. 11c), producing a deceleration effect on the mean flow above and an acceleration effect below. Figure 11b shows that deceleration does take place at the upper levels, but only a slight acceleration appears near the surface. This suggests that the horizontal momentum transport is also important at the lower levels. We further investigate this situation in the rest of this subsection.

With the use of the definition of vorticity given by (6), the anelastic continuity equation given by (1), and the cyclic continuity in x, we can derive the following relation between the zonally averaged flux convergence of zonal momentum and vorticity transports by the thermal:

$$-\left[\frac{\partial}{\rho_0 \partial y}(\rho_0 \overline{u'v'}^x) + \frac{\partial}{\rho_0 \partial z}(\rho_0 \overline{u'w'}^x)\right] = -\overline{w'\eta'}^x + \overline{v'\zeta'}^x. \tag{28}$$

The relation (28) is expected to hold approximately even without a cyclic condition if the averaging is over a domain bounded by the relatively calm environment. The relation (28) gives an alternative way of viewing parameterization of cumulus friction as a problem of vorticity transports by cumulus convection.

The top panels in Fig. 12 show the zonally and time-averaged vertical and horizontal momentum fluxes by the deviation from the zonal mean. Clearly, the vertical momentum transport is downgradient near the center of the y domain representing the region of active convection, while weaker upgradient transports appear in the nearby regions. The middle panels in Fig. 12 show the corresponding flux convergences of momentum representing the two terms in the left-hand side of (28).

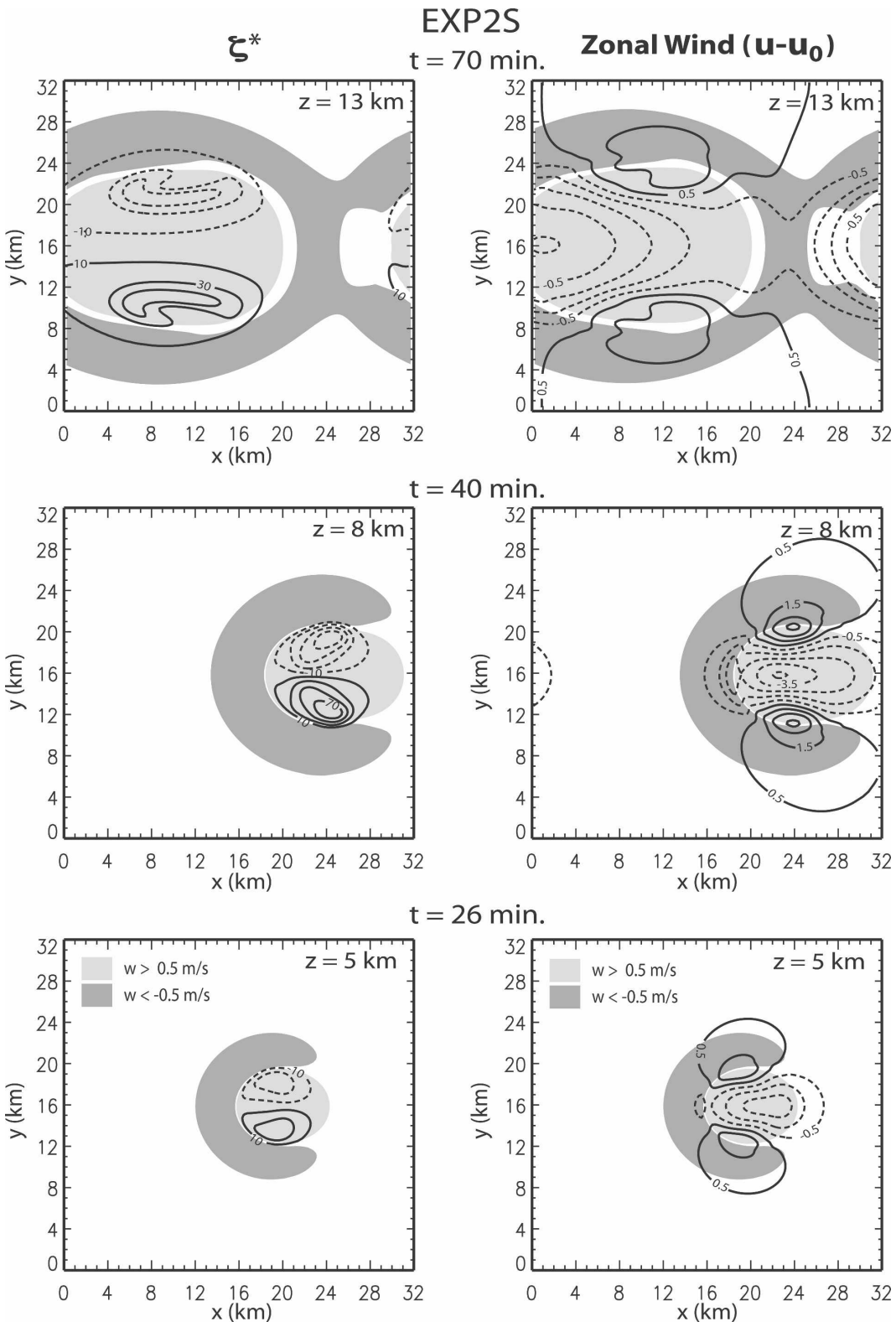

FIG. 8. The (left) ζ^* ($\equiv \zeta/\rho_o$) field and (right) zonal wind on the x–y cross section obtained from EXP2S. The solid and dashed lines represent positive and negative values, respectively. The contour intervals are (left) 20×10^{-4} m^3 kg^{-1} s^{-1} and (right) 1 m s^{-1}. The updraft and downdraft are shaded light gray and dark gray, respectively.

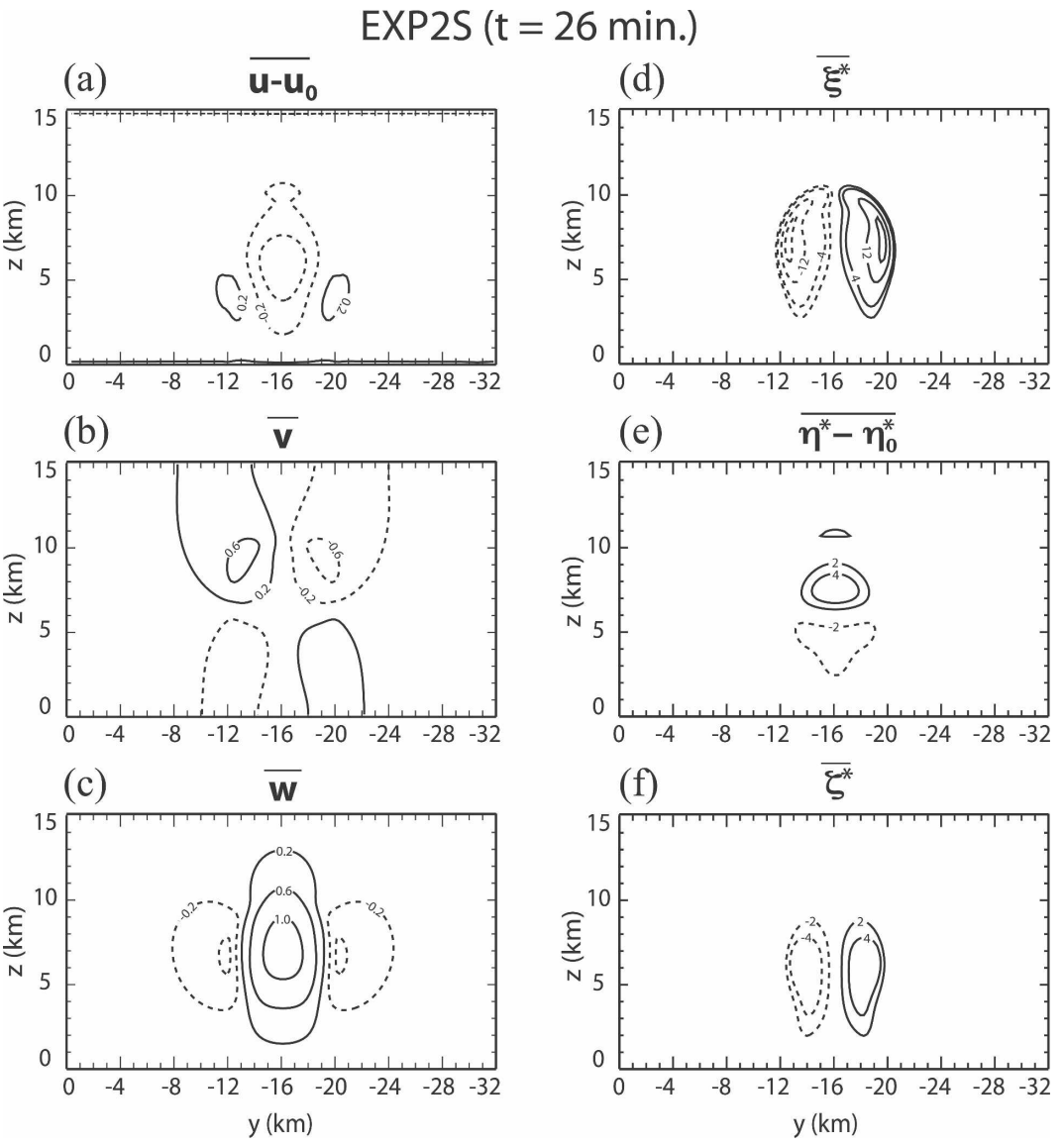

FIG. 9. Zonally averaged (a) x, (b) y, and (c) z components of velocity and (d) ξ^*, (e) η^*, and (f) ζ^* fields on the y–z cross section obtained from EXP2S at $t = 26$ min. The solid and dashed lines represent positive and negative values, respectively. The contour interval in (a)–(c) is 0.4 m s^{-1} and the contours in (d)–(f) are ± 2, ± 4, ± 12, ± 20, . . . (10^{-4} m^3 kg^{-1} s^{-1}).

Here we see the tendency toward compensation by the vertical and horizontal convergences. At the upper levels near the center of the y domain, a significant part of the deceleration due to the downward momentum transport is canceled by the acceleration due to the horizontal momentum transport. At the lower levels near the center of the y domain, on the other hand, the acceleration effect due to the downward momentum transport is almost entirely canceled by the deceleration due to the horizontal momentum transport.

The bottom panels in Fig. 12 show the zonally and time-averaged vertical flux of η and the zonally and time-averaged horizontal flux of ζ. These fluxes represent the terms in the right-hand side of (28). At the middle levels, the upward transport of η near the center of the y domain represents the deceleration in the convectively active region. At the lower levels, the positive horizontal transport of ζ off the center of the y domain represents acceleration in the neighboring convectively inactive region. In this way, unlike the momentum flux convergences, the effects of individual vorticity transports dominate at different places in the vertical cross

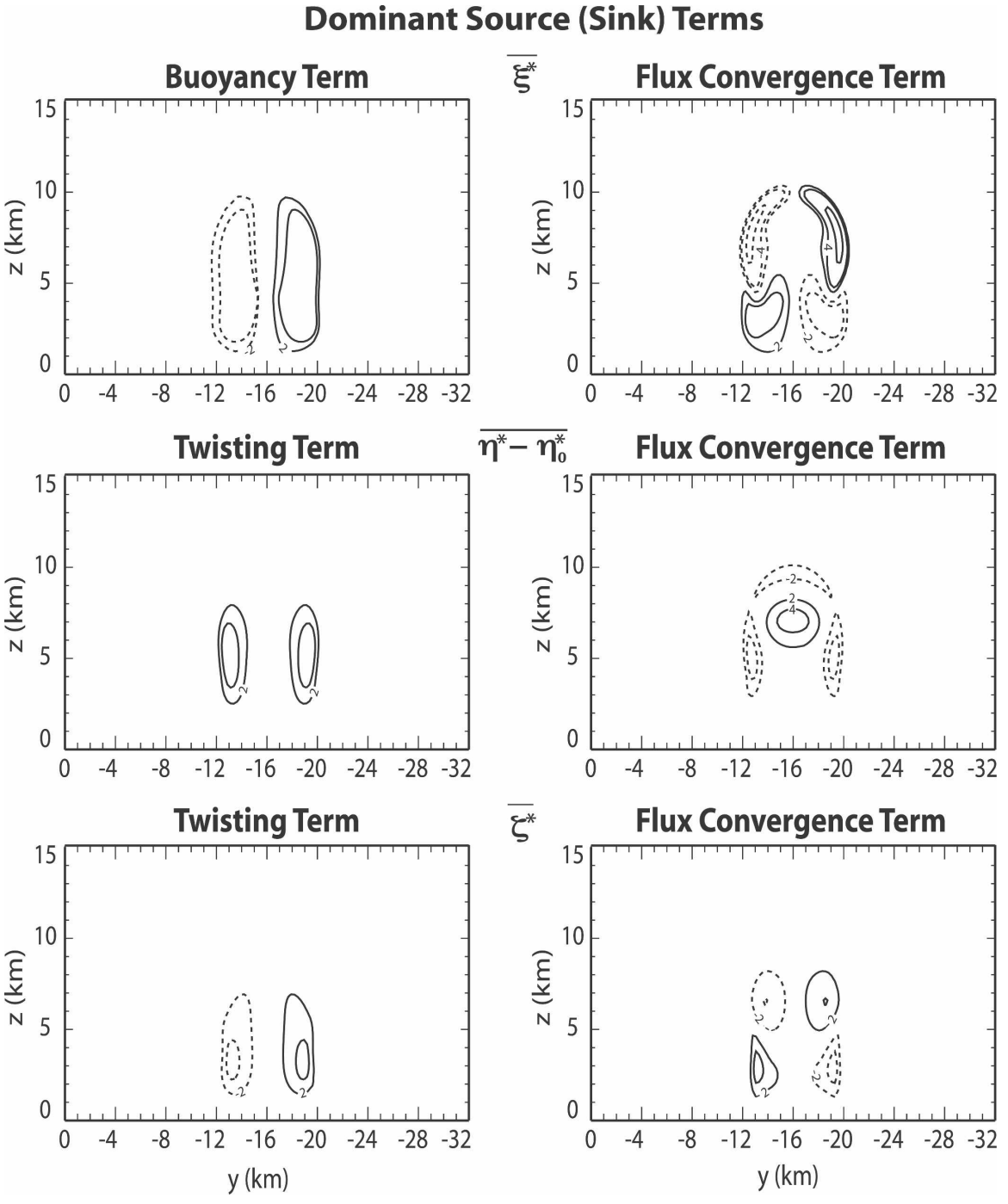

FIG. 10. Zonally averaged dominant source (sink) terms for (top) ξ^*, (middle) η^*, and (bottom) ζ^* in (8), (9), and (10) obtained from EXP2S. These are accumulated effects from $t = 0$ to $t = 26$ min. The solid and dashed lines represent positive and negative values, respectively. The contours are ± 2, ± 4, ± 12, ± 20, ... (10^{-4} m^3 kg^{-1} s^{-1}).

section with no clear tendency for mutual compensation. This means that an analysis of the vorticity transports presents a clearer view of the acceleration/deceleration processes than that of the momentum flux convergences.

4. Experiments with physics

To simulate the development of an ensemble of clouds using the model with full physics, which includes microphysics, radiation, and turbulence, two experi-

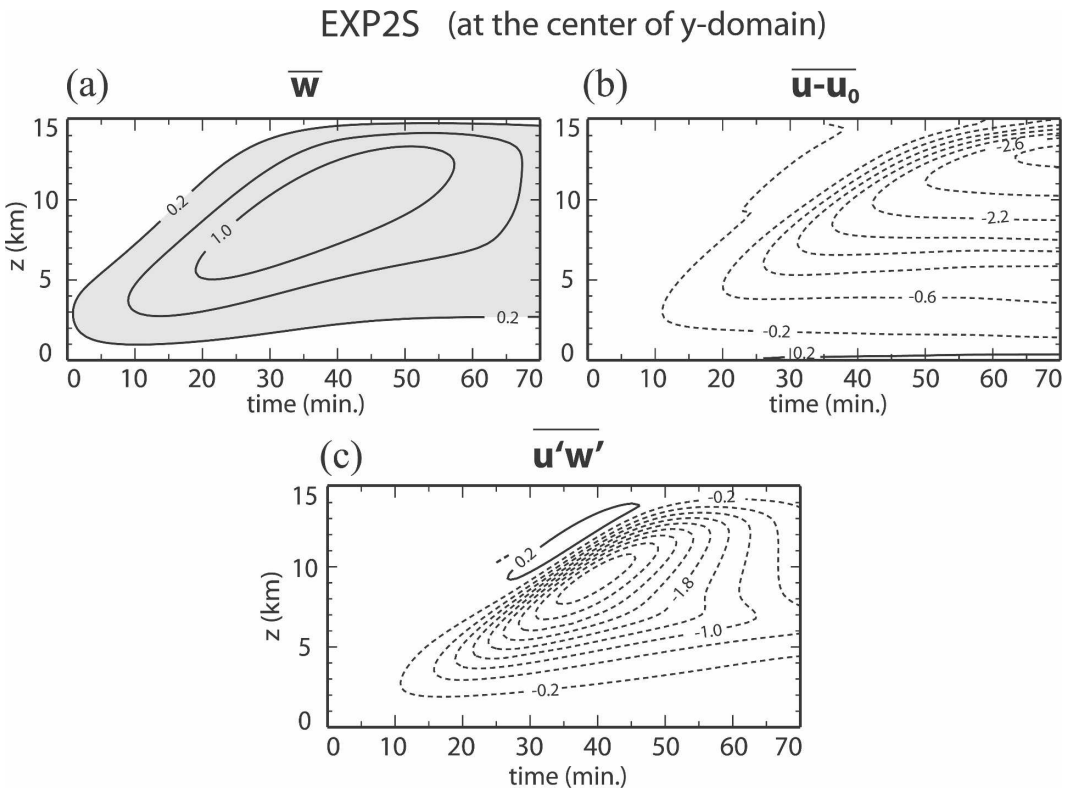

FIG. 11. Zonally averaged (a) vertical and (b) zonal velocities and (c) vertical eddy momentum flux on the z–t cross section at the center of the y domain obtained from EXP2S. The solid and dashed lines represent positive and negative values, respectively. The contour intervals are (a), (b) 0.4 m s^{-1} and (c) 0.4 m^2 s^{-2}.

ments are performed; EXP3 with no shear and EXP3S with shear. The model is applied to a 512 km × 512 km horizontal domain with a 2-km horizontal grid size. In the vertical, the model has 34 levels based on the stretched vertical grid with a top at 18 km. The vertical grid size ranges from about 100 m near the surface to about 1000 m near the model top. The upper and lower boundaries are rigid and the lateral boundaries are cyclic. The Coriolis parameter at 15°N is used. The model also includes a Newtonian-type cooling above the 10-km height to maintain realistic climatology of the stratosphere and a Rayleigh-type friction in the top five layers to absorb upward-propagating gravity waves.

An idealized ocean surface condition is used, in which the surface temperature is prescribed as 299.8 K. The cosine of the solar zenith angle is fixed to 0.5, representing a typical daytime condition in the Tropics. The initial thermodynamic state and zonal wind fields are selected idealizing the Global Atmospheric Research Program (GARP) Atlantic Tropical Experiment (GATE) phase III conditions. Figure 13 shows the initial profiles of moist static energy and zonal wind. The y component of wind is initially set to zero. To maintain the mean wind shear, the area mean of horizontal wind is fixed to its initial value throughout the simulation periods of EXP3 and EXP3S. Thus, (18) and (19) are not used. Clouds are initiated by small random potential temperature perturbations introduced into the lowest model layer over the 15-min period after the first 5 min of the integration. Large-scale forcing representing the climatological background is imposed on the model through prescribed cooling and moistening rates (Fig. 14). The integration period is 48 h and the time step is 10 s.

Development of the cloud ensemble during the period can be seen in Fig. 15 (EXP3) and Fig. 16 (EXP3S). Theses figures show the distribution of the cloud-top temperature in the x–y domain with a 16-h interval. The cloud top is defined as the layer where the path of liquid water and ice [i.e., $\int(q_c + q_i)\rho\, dz$] first exceeds 0.1 kg m^{-2} when integrated downward from the model top, where q_c is the mixing ratio of cloud liquid water and q_i is that of ice. In these figures, cirrus anvils associated with cumulonimbi appear white and there are no clouds in black areas. For both experiments, clouds develop nearly everywhere in the early stage of the simulation because the integration starts from a horizontally uniform and conditionally unstable condition. As time progresses, clouds develop differently in EXP3 and

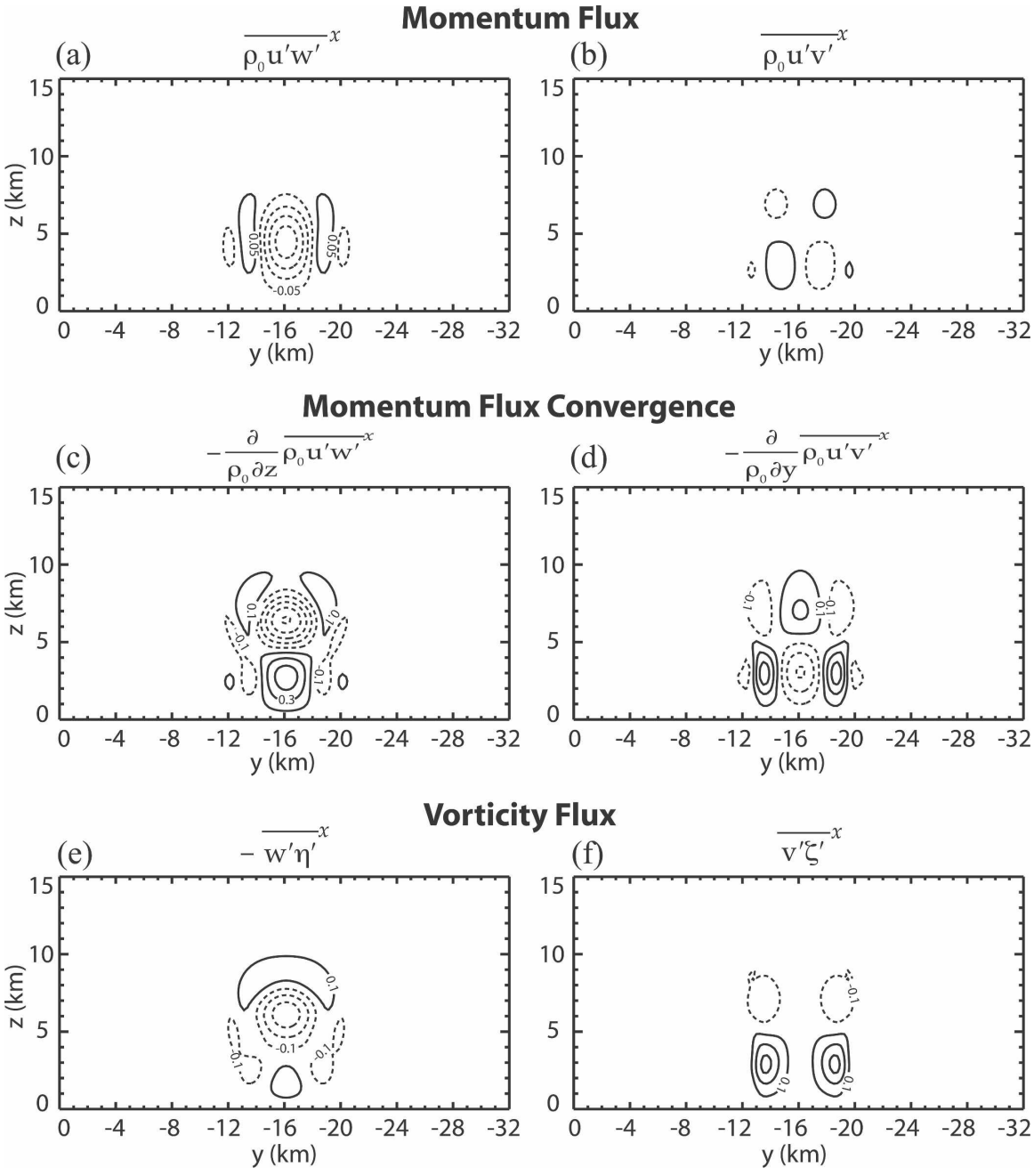

FIG. 12. The zonally and time-averaged (a) vertical and (b) meridional fluxes of zonal momentum, (c) vertical and (d) meridional flux convergences of zonal momentum, (e) vertical flux of the *y* component of vorticity, and (f) meridional flux of the *z* component of vorticity due to cumulus convection obtained from EXP2S. The time average is taken over the first 26 min. Solid and dashed lines represent positive and negative values, respectively. The contour intervals are (a), (b) 0.1 kg m^{-1} s^{-2} and (c)–(f) 0.2 m s^{-1} h^{-1}.

EXP3S. With shear (EXP3S), several organized systems develop (Fig. 16), which consist of narrow convective bands aligned mostly parallel to the shear vector. Behind the bands, there are broad areas of midlevel stratiform clouds. Without shear (EXP3), on the contrary, no mesoscale bandlike cloud organizations develop (Fig. 15).

The domain- and time-averaged profiles of the vertical flux convergence of zonal momentum and the fluxes of vorticity components due to cumulus convection obtained from EXP3S are shown in Fig. 17. Here, the time average is taken over the 2-day simulation period. Figure 17a shows a layer of the westerly momentum flux convergence above the level of the

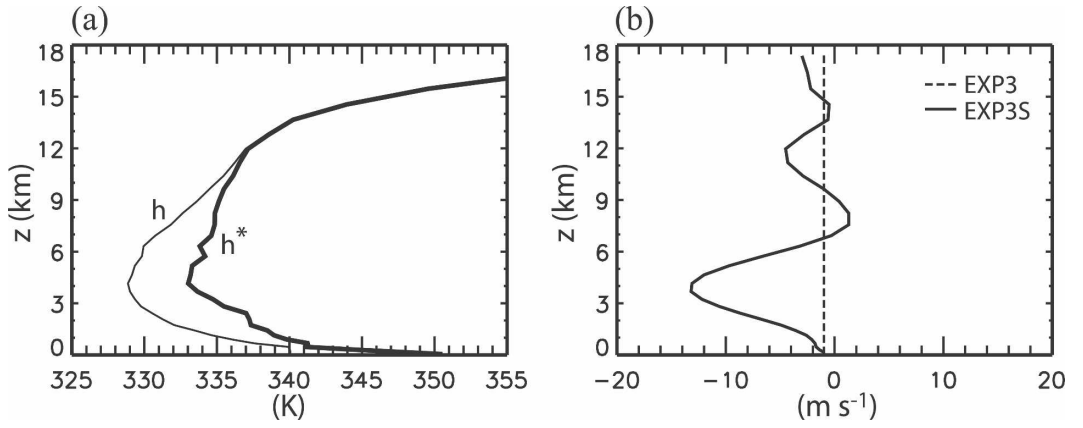

FIG. 13. Initial profiles of (a) moist static energy (h^*; saturation moist static energy) divided by c_p and (b) zonal wind used in EXP3 and EXP3S, where c_p is the specific heat of dry air.

midtropospheric easterly jet core shown in Fig. 13b, and a layer of easterly momentum flux convergence below the jet core. Although our experiment is highly idealized, especially because the mean zonal wind and large-scale forcing are fixed in time to represent only the mean GATE phase III condition, the result is consistent with those by Sui and Yanai (1986) and Mapes and Wu (2001).

Finally, we present the result from EXP3S in view of the deceleration (acceleration) effect of the vorticity transport on the domain-averaged zonal wind. Averaging (28) and using the cyclic condition in y, we obtain

$$-\frac{\partial}{\rho_0 \partial z}(\rho_0 \overline{u'w'}) = -\overline{w'\eta'} + \overline{v'\zeta'}, \tag{29}$$

where, unlike in (28), the overbar and prime indicate the horizontal average *over the entire model domain* and the deviation, respectively. When the y component of vorticity is transported upward (downward), there is a deceleration (acceleration) tendency of westerly wind. On the other hand, when the z component of vorticity is transported leftward (rightward) as seen from above, there is an acceleration (deceleration) tendency of the westerly wind. Figure 17b shows that the latter effect is negligible in this case. Then, as expected from (29), the vertical momentum flux convergence and the vertical vorticity transport are approximately equal. It should be remembered, however, that this does not hold for more local convection as we pointed out earlier, for which the effects of horizontal transports must be considered as in (28).

5. Summary and conclusions

This paper describes a newly developed three-dimensional anelastic model based on the vorticity equation, which has a completely different logical structure for dynamics from the models based on the momentum equation. In this model, the prognostic variables of the model are the horizontal components of vorticity, potential temperature and mixing ratios of various phases of water at all heights, and the vertical component of vorticity and the horizontally uniform part of horizontal velocity at a selected height. With the use of an expression for the nondivergence of the vorticity vector, the vertical component of vorticity at the other heights is diagnostically determined. The nonuniform part of horizontal velocity at the selected height is obtained by solving the two-dimensional Poisson-type equations for streamfunction and velocity potential. The horizontal velocity at the other heights is then updated from the predicted vorticity fields and the veloc-

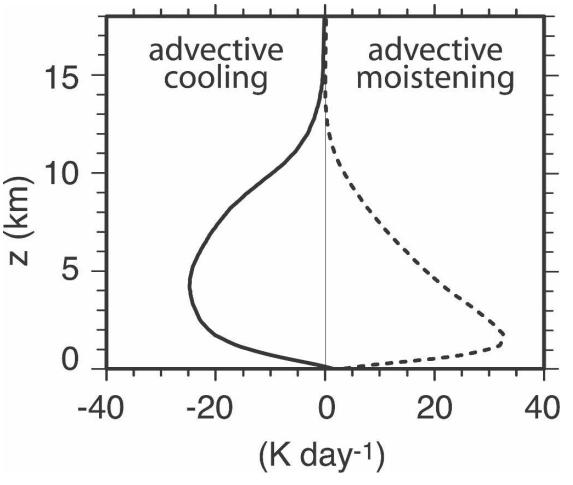

FIG. 14. Vertical profiles of the prescribed large-scale advective cooling and moistening rates used in EXP3 and EXP3S. Here, the moistening rate is multiplied by L/c_p, where L is the latent heat of condensation.

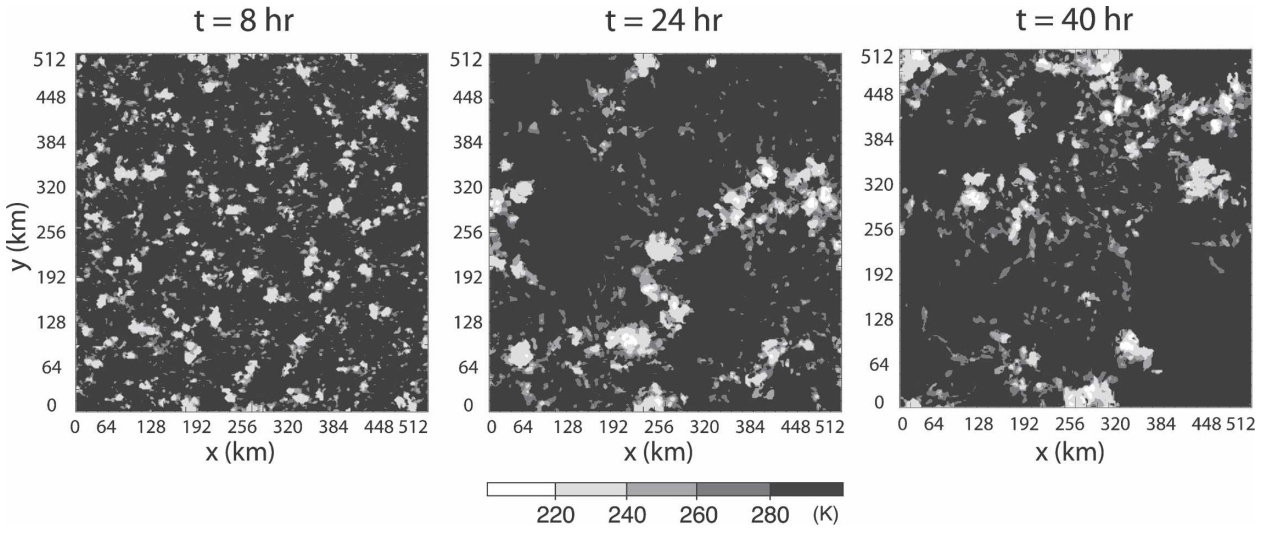

FIG. 15. Time evolution of cloud-top temperature in the *x*–*y* domain obtained from EXP3.

ity obtained at the selected height. For the vertical velocity, a three-dimensional elliptic equation is solved with prescribed vertical boundary conditions. This procedure replaces solving the elliptic equation for the perturbation pressure in the standard anelastic system based on the momentum equation. For advection of vorticity and scalar variables, the model uses a partially third-order scheme. When time is continuous, this scheme is quadratically bounded.

As an application of the model, interactions between convection and its environment with vertical shear are studied without and with model physics through the viewpoint of vorticity dynamics, the deceleration/acceleration process of basic flow in particular. In the warm bubble experiments, it is shown that the buoyant thermal under the basic shear flow induces local wind deceleration through the twisting effects on the vorticity components. This local wind deceleration is associated with the generation of a couplet of the vertical component of vorticity in the horizontal plane. The budget analysis of vorticity also shows that three-dimensional advection is as important as the twisting effects in the distribution of the vorticity couplet.

The model is then tested with simulations of ensemble clouds using the full physics in a large domain for environments with no shear (EXP3) and with shear (EXP3S). The simulation with sheared environment shows the development of mesoscale bandlike organi-

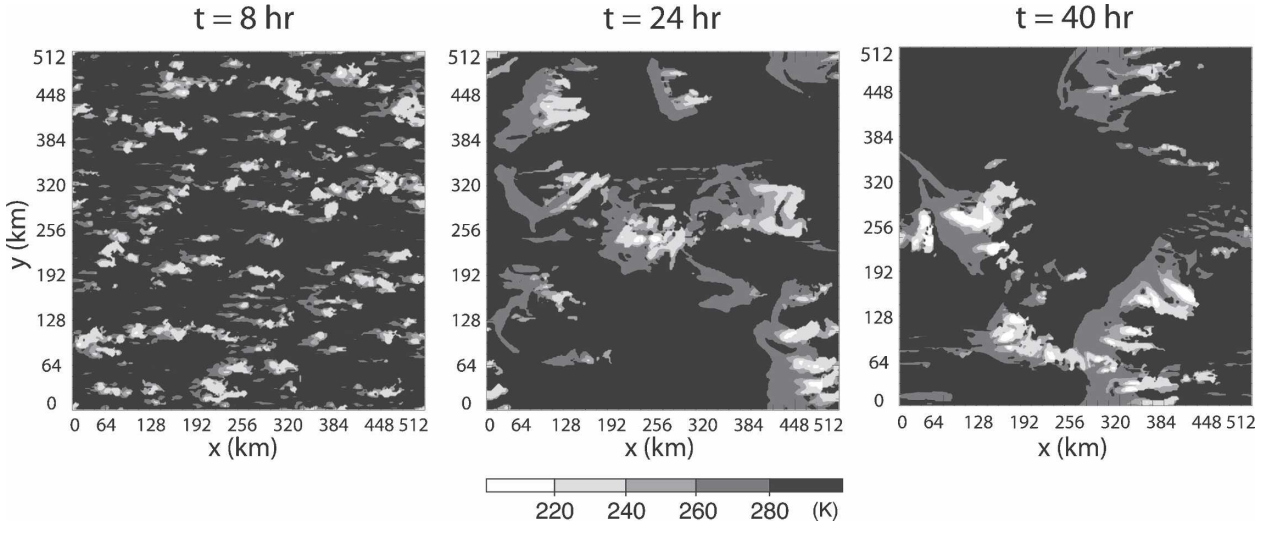

FIG. 16. Same as in Fig. 15, but obtained from EXP3S.

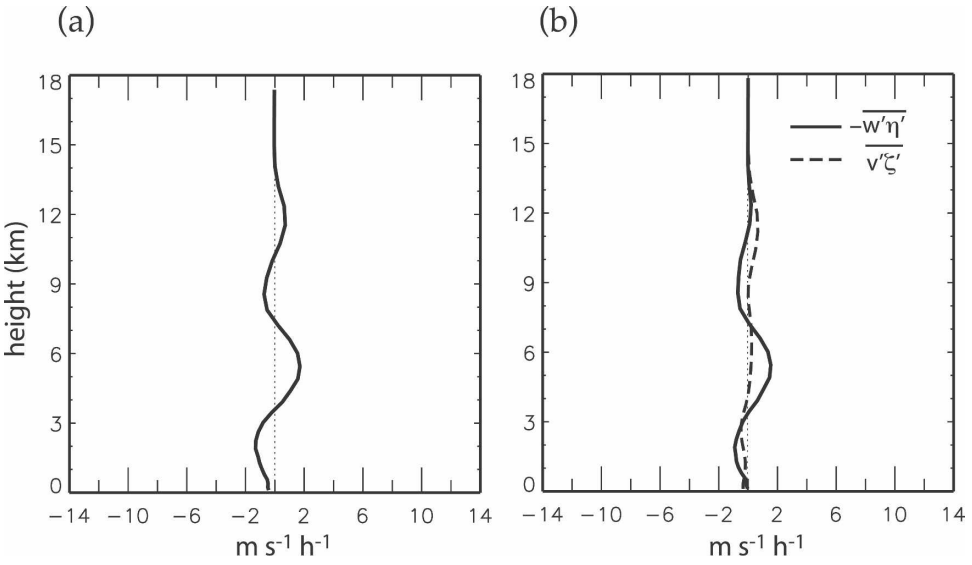

FIG. 17. Domain- and time-averaged profiles of (a) the vertical flux convergence of zonal momentum and (b) the fluxes of vorticity components due to cumulus convection obtained from EXP3S. The time average is taken over the 2-day simulation period.

zation of clouds. Although our simulation is highly idealized, especially because the mean zonal wind and large-scale forcing are fixed in time to represent only the mean GATE phase III condition, an analysis of the components responsible for the time change of the domain-averaged zonal momentum shows that the results are consistent with the earlier studies. Comparisons of (28) with (29) and Fig. 12 with Fig. 17 suggest that the cumulus friction problem should be treated as a purely three-dimensional problem when we are concerned with the effect of relatively local features associated with cumulus activity. In this case, looking at the problem from the point of view of vorticity transports gives a clearer picture than that of the momentum flux convergence. On the other hand, when the cumulus activity is spread over a large domain and when we are only concerned with the area average over a large domain, the two ways of viewing the problem do not make an essential difference. These results confirm that parameterization of the cumulus friction problem for large-scale models is a resolution-dependent problem.

For future development of the current model, we are planning to introduce bottom topography, possibly with the change of the vertical grid from the Lorenz grid to the Charney–Phillips grid [for comparison of these grids, see, e.g., Arakawa and Konor (1996)]. We are also planning to develop a version of the model in which the computational constraint by the elliptic equation due to the use of the anelastic approximation is relaxed to avoid global calculations. Another modification we are planning is to generalize the system of the anelastic equations while maintaining the structure of the model based on the three-dimensional vorticity equation. In its original form, the anelastic approximation requires that the reference state be either isentropic or near isentropic (Ogura and Phillips 1962; Lipps and Hemler 1982). Durran (1989) and Bannon (1996) presented revised anelastic systems that are not subject to such constraints while conserving energy. Currently we are developing a model that unifies the standard quasistatic model for large scales, which partially includes compressibility, and a generalization of the pseudoincompressible approximation proposed by Durran (1989) for small scales.

Acknowledgments. We thank Professor David Randall for his support of this work and useful comments on the original manuscript. We also thank Dr. William Skamarock and other reviewers for their constructive comments and suggestions. This research was supported by the U.S. DOE through Grants DE-FG02-02ER63370 to the Colorado State University (CSU), DE-FC02-01ER63163 to CSU (in part given to the CSU Contract G-3816-3 to UCLA), and DE-FC02-06ER64302 to Colorado State University (in part given to the CSU Contract G-3818-1 to UCLA), from the NSF through Grants ATM-0415184 and ATM-0425247 (CMMAP) to CSU (in part given to the CSU Contract G-3045-1 to UCLA), and also from NASA through Grant NNG04GA76G to UCLA.

REFERENCES

Arakawa, A., and C. S. Konor, 1996: Vertical differencing of the primitive equations based on the Charney–Phillips grid in hybrid σ–p vertical coordinates. *Mon. Wea. Rev.,* **124,** 511–528.

Bannon, P., 1996: On the anelastic approximation for a compressible atmosphere. *J. Atmos. Sci.,* **53,** 3618–3628.

Cho, H. R., and T. L. Clark, 1981: A numerical investigation of the structure of vorticity fields associated with a deep convective cloud. *Mon. Wea. Rev.,* **109,** 1654–1670.

Clark, T. L., 1979: Numerical simulations with a three-dimensional cloud model: Lateral boundary condition experiments and multicellular severe storm simulations. *J. Atmos. Sci.,* **36,** 2191–2215.

Cotton, W. R., and G. J. Tripoli, 1978: Cumulus convection in shear flow—Three-dimensional numerical experiments. *J. Atmos. Sci.,* **35,** 1503–1521.

Deardorff, J. W., 1972: Parameterization of the planetary boundary layer for use in general circulation models. *Mon. Wea. Rev.,* **100,** 93–106.

Durran, D. R., 1989: Improving the anelastic approximation. *J. Atmos. Sci.,* **46,** 1453–1461.

Fu, Q., S. K. Krueger, and K. N. Liou, 1995: Interactions of radiation and convection in simulated tropical cloud clusters. *J. Atmos. Sci.,* **52,** 1310–1328.

Jung, J.-H., and A. Arakawa, 2005: A three-dimensional cloud model based on the vector vorticity equation. Colorado State University Atmospheric Science Paper 762, 57 pp. [Available online at http://kiwi.atmos.colostate.edu/pubs/joon-hee-tech_report.pdf.]

Khairoutdinov, M. F., and D. A. Randall, 2003: Cloud resolving modeling of the ARM summer 1997 IOP: Model formulation, results, uncertainties, and sensitivities. *J. Atmos. Sci.,* **60,** 607–625.

Kirk, J. R., 2003: Comparing the dynamical development of two mesoscale convective vortices. *Mon. Wea. Rev.,* **131,** 862–890.

Klemp, J. B., and R. B. Wilhelmson, 1978: The simulation of three-dimensional convective storm dynamics. *J. Atmos. Sci.,* **35,** 1070–1096.

Kogan, Y. L., 1991: The simulation of a convective cloud in a 3-D model with explicit microphysics. Part I: Model description and sensitivity experiments. *J. Atmos. Sci.,* **48,** 1160–1189.

Krueger, S. K., 1988: Numerical simulation of tropical cumulus clouds and their interaction with the subcloud layer. *J. Atmos. Sci.,* **45,** 2221–2250.

——, 2000: Cloud system modeling. *General Circulation Model Development: Past, Present, and Future,* D. A. Randall, Ed., Academic Press, 605–640.

——, Q. Fu, K. N. Liou, and H.-N. Chin, 1995: Improvements of an ice-phase microphysics parameterization for use in numerical simulations of tropical convection. *J. Appl. Meteor.,* **34,** 281–287.

Lin, Y.-L., R. D. Farley, and H. D. Orville, 1983: Bulk parameterization of the snow field in a cloud model. *J. Climate Appl. Meteor.,* **22,** 1065–1092.

Lipps, F. B., and R. S. Hemler, 1982: A scale analysis of deep moist convection and some related numerical calculations. *J. Atmos. Sci.,* **39,** 2192–2210.

——, and ——, 1986: Numerical simulation of deep tropical convection associated with large-scale convergence. *J. Atmos. Sci.,* **43,** 1796–1816.

Lord, S. J., H. E. Willoughby, and J. M. Piotrowicz, 1984: Role of a parameterized ice-phase microphysics in an axisymmetric, nonhydrostatic tropical cyclone model. *J. Atmos. Sci.,* **41,** 2836–2848.

Mapes, B. E., and X. Wu, 2001: Convective eddy momentum tendencies in long cloud-resolving model simulations. *J. Atmos. Sci.,* **58,** 517–526.

Miller, M. J., and R. P. Pearce, 1974: A three-dimensional primitive equation model of cumulonimbus convection. *Quart. J. Roy. Meteor. Soc.,* **100,** 133–154.

Ogura, Y., and N. A. Phillips, 1962: Scale analysis of deep and shallow convection in the atmosphere. *J. Atmos. Sci.,* **19,** 173–179.

Redelsperger, J.-L., and G. Sommeria, 1986: Three-dimensional simulation of a convective storm: Sensitivity studies on subgrid parameterization and spatial resolution. *J. Atmos. Sci.,* **43,** 2619–2635.

Rotunno, R., 1981: On the evolution of thunderstorm rotation. *Mon. Wea. Rev.,* **109,** 577–586.

Saitoh, T. S., T. Shimada, and H. Hoshi, 1996: Modeling and simulation of the Tokyo urban heat island. *Atmos. Environ.,* **30,** 3431–3442.

Schlesinger, R. E., 1978: A three-dimensional numerical model of an isolated thunderstorm: Part I. Comparative experiments for variable ambient wind shear. *J. Atmos. Sci.,* **35,** 690–713.

——, 1980: A three-dimensional numerical model of an isolated thunderstorm. Part II: Dynamics of updraft splitting and mesovortex couplet evolution. *J. Atmos. Sci.,* **37,** 395–420.

Shutts, G. J., and M. E. B. Gray, 1994: A numerical modeling study of the geostrophic adjustment process following deep convection. *Quart. J. Roy. Meteor. Soc.,* **120,** 1145–1178.

Sievers, U., and W. G. Zdunkowski, 1986: A microscale urban climate model. *Beitr. Phys. Atmos.,* **59,** 13–40.

Skamarock, W. C., M. L. Weisman, and J. B. Klemp, 1994: Three-dimensional evolution of simulated long-lived squall lines. *J. Atmos. Sci.,* **51,** 2563–2584.

Steiner, J. T., 1973: A three-dimensional model of cumulus cloud development. *J. Atmos. Sci.,* **30,** 414–435.

Straka, J. M., R. B. Wilhelmson, L. J. Wicker, J. R. Anderson, and K. K. Droegemeier, 1993: Numerical solutions of a non-linear density current: A benchmark solution and comparisons. *Int. J. Numer. Methods Fluids,* **17,** 1–22.

Sui, C.-H., and M. Yanai, 1986: Cumulus ensemble effects on the large-scale vorticity and momentum fields of GATE. Part I: Observational evidence. *J. Atmos. Sci.,* **43,** 1618–1642.

Takahashi, T., 1981: Warm rain development in a three-dimensional cloud model. *J. Atmos. Sci.,* **38,** 1991–2013.

Tao, W.-K., and S.-T. Soong, 1986: A study of the response of deep tropical clouds to mesoscale processes: Three-dimensional numerical experiments. *J. Atmos. Sci.,* **43,** 2653–2676.

Thunis, P., and A. Clappier, 2000: Formulation and evaluation of a nonhydrostatic mesoscale vorticity model (TVM). *Mon. Wea. Rev.,* **128,** 3236–3251.

Thyer, N. H., 1966: A theoretical explanation of mountain and valley winds by a numerical model. *Arch. Meteor. Geophys. Bioklimatol.,* **26,** 39–50.

Tollerud, E. I., and S. K. Esbensen, 1983: An observational study of the upper-tropospheric vorticity fields in GATE cloud clusters. *Mon. Wea. Rev.,* **111,** 2161–2175.

Weisman, M. L., and R. Rotunno, 2004: "A theory for strong long-lived squall lines" revisited. *J. Atmos. Sci.,* **61,** 361–382.